nature materials

Article

https://doi.org/10.1038/s41563-023-01787-8

Compensating losses in polariton propagation with synthesized complex frequency excitation

Received: 23 July 2023

Accepted: 11 December 2023

Published online: 8 January 2024

Check for updates

Fuxin Guan[1,5], Xiangdong Guo[1,2,5], Shu Zhang[2,5], Kebo Zeng[1], Yue Hu[1], Chenchen Wu[2], Shaobo Zhou[1], Yuanjiang Xiang[3], Xiaoxia Yang[2], Qing Dai[2] ✉ & Shuang Zhang[1,4] ✉

Surface plasmon polaritons and phonon polaritons offer a means of surpassing the diffraction limit of conventional optics and facilitate efficient energy storage, local field enhancement and highsensitivity sensing, benefiting from their subwavelength confinement of light. Unfortunately, losses severely limit the propagation decay length, thus restricting the practical use of polaritons. While optimizing the fabrication technique can help circumvent the scattering loss of imperfect structures, the intrinsic absorption channel leading to heat production cannot be eliminated. Here, we utilize synthetic optical excitation of complex frequency with virtual gain, synthesized by combining the measurements made at multiple real frequencies, to compensate losses in the propagations of phonon polaritons with dramatically enhanced propagation distance. The concept of synthetic complex frequency excitation represents a viable solution to the loss problem for various applications including photonic circuits, waveguiding and plasmonic/phononic structured illumination microscopy.

Polaritons, including surface plasmon polaritons (SPPs)[1–3] and phonon polaritons (PhPs)[4,5], have emerged as highly promising candidates for constructing nanophotonic circuits[6–8], enabling the development of ultracompact and high-speed optical devices. Utilizing polaritons in nanophotonics provides a pathway to overcoming the diffraction limit of light, allowing for the control of light at the nanoscale[9–11]. However, the intrinsic losses have hindered many loss-sensitive applications based on polaritons[12], including waveguiding[13], biosensing[14–17], sub-diffraction-limit imaging[18–21] and plasmonic structured illumination microscopy[22]. Intrinsic loss negatively impacts polaritons in two primary ways: (1) the propagation distances are significantly reduced, and (2) the dispersion curves of polaritons far from the light cone are strongly blurred, which severely affects the applications of subwavelength behaviours of polaritons.

The intrinsic loss is caused by the imaginary part of the dielectric function in a material, such as the Ohmic loss in plasmon systems and the lattice vibration relaxation process in phonon-polariton systems[23,24]. The most commonly used method to offset loss is to incorporate an external gain medium[25–27]. However, it is very challenging to completely offset the plasmonic loss with gain, and gain compensation[28–30] is susceptible to noises and instabilities.

Complex frequency waves with virtual gain have been proposed to counteract losses in plasmonic/phononic materials for various applications, including super-resolution imaging[31–33], long-range propagation[34], slow light[35–38], coherent virtual absorption[39], light superscattering[40] and virtual parity-time symmetry[41]. The concept of complex frequency waves has also been extended to acoustic systems[42].

[1]New Cornerstone Science Laboratory, Department of Physics, University of Hong Kong, Hong Kong, China. [2]CAS Key Laboratory of Nanophotonic Materials and Devices, CAS Key Laboratory of Standardization and Measurement for Nanotechnology, CAS Center for Excellence in Nanoscience, National Center for Nanoscience and Technology, Beijing, China. [3]School of Physics and Electronics, Hunan University, Changsha, China. [4]Department of Electrical & Electronic Engineering, University of Hong Kong, Hong Kong, China. [5]These authors contributed equally: Fuxin Guan, Xiangdong Guo, Shu Zhang. ✉e-mail: daiq@nanoctr.cn; shuzhang@hku.hk

https://doi.org/10.1038/s41563-023-01787-8

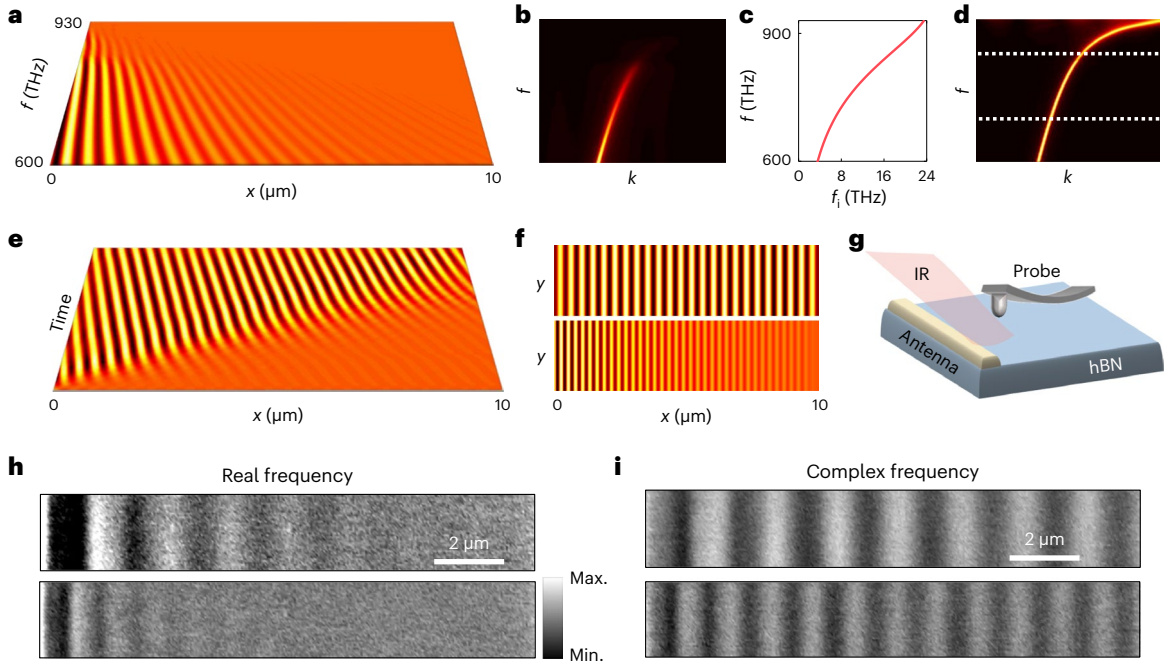

Fig. 1 | Concept of loss-compensation for polariton propagation using synthetic wave of complex frequency. a, SPP propagation distribution as a function of frequency launched by an infinitely long antenna. **b**, The corresponding Fourier distribution of the propagation field, where the wave vector (x-axis) ranges from 0 to 42.4 μm^{-1}, and the frequency (y axis) ranges from 600 THz to 930 THz. **c**, The imaginary part of the complex frequency, i.e., virtual gain, as a function of its real part derived from equation (1). **d**, The synthetic Fourier distribution in the complex frequency domain under the condition Im(k) = 0. **e**, The spatiotemporal dynamics at complex frequency excitation of (700 - 6.73i) THz, with its real part indicated by the lower dashed line position in **d**. **f**, The electric field distribution at (700 - 6.73i) THz (top) and (850 - 17i) THz (bottom), as indicated by the two dashed lines in **d**. **g**, Schematic of s-SNOM experimental set-up with a gold antenna on top of an hBN flake. Illumination on the antenna excites the PhPs and electric field distribution is measured by the probe. **h**, The near-field distributions at two real frequencies of 1,451 cm^{-1} and 1,477 cm^{-1}. **i**, The corresponding complex frequency near-field distributions. Bright and dark colours correspond to maximum and minimum values.

Complex frequency waves feature temporal attenuation, which requires a precise exponential decay profile in time and time-gated measurements, which are challenging for experimental implementation in optics. Recent research has introduced a multifrequency approach to synthesizing the system response under complex frequency excitation in experiment by combining multiple real frequency measurements[32], which has shown promise in restoring the imaging performance of superlenses, typically degraded by intrinsic losses.

Here, we demonstrate the compensation of propagation loss for highly confined PhPs via virtual gain, implemented by the complex frequency approach. The key to the compensation of the propagation loss lies in the offsetting of the imaginary part of the in-plane wavevector instead of the imaginary part of the permittivity, which is implemented in the mid-infrared regime. Furthermore, our results provide insight into the wave-packet dynamics of spatiotemporal evolution of the polariton propagation, with the propagation length of the complex frequency signal much longer than that of the real frequency. This opens up new possibilities for various applications such as photonic integrated circuits, biosensing and microscopy.

Typical materials that support SPPs/PhPs can be described by the Drude model, Lorentz model or multi-Lorentz model[43], which contain loss terms that result in the imaginary part of the in-plane wavevector. The wavevector is dependent on frequency, and thus a certain imaginary part of the complex frequency is required to offset the imaginary part of the in-plane wavevector. For simplicity, we start with an example of SPPs at an interface, whose mathematical solution is given by $k = \omega\sqrt{\varepsilon_m}/(c\sqrt{1+\varepsilon_m})$ with $\boldsymbol{k}$ denoting the SPP wavevector, where we assume that the permittivity of plasmonic metal is described by a Drude model $\varepsilon_m = \varepsilon_r - \omega_p{}^2/(\omega^2 + i\omega\gamma)$ with ε_r, ω_p and γ corresponding to the dielectric constant at infinite frequency, plasma frequency and dissipation term, respectively. The dissipation term in the denominator introduces decay to the propagation of SPPs. It is intuitive to think that the complete compensation of the propagation loss of SPPs could be achieved by fully compensating the loss in the Drude model with a specific complex frequency $\tilde{\omega} = \omega - i\gamma/2$. However, this is not entirely accurate, as there is still a frequency-dependent term $\tilde{\omega}$ in the dispersion formula that can result in an imaginary component on wavevectors. The true condition for complete loss compensation is indeed given by Im(k) = 0, which leads to

$$\beta \approx \gamma\omega_p^2\omega^2/\left(2\left(\omega_p^2 - \varepsilon_r\omega^2\right)^2 + 2\varepsilon_r\omega^4\right) \quad (1)$$

where $\tilde{\omega} = \omega - i\beta$, ω corresponds to the central frequency and β represents the virtual gain, with details of the derivation provided in Supplementary Section 1. The loss compensation condition for a Lorentz model $\varepsilon_m = \varepsilon_r - \omega_p{}^2/(\omega^2 + i\omega\gamma - \omega_0{}^2)$ is also provided in Supplementary Section 1, where ω_0 is the resonance frequency. This condition ensures that the imaginary part of the wavevector is zero, which in turn implies that there is no spatial growth or decay of the SPPs along the interface. Therefore, to achieve a complete loss compensation for the polariton propagation, it is necessary to find appropriate values for the imaginary part of the frequency.

As an example, we assume a realistic plasmonic metal described by the Drude model with $\varepsilon = 5 - \omega_p{}^2/(\omega^2 + i\omega\gamma)$, where $\omega_p = 1.442 \times 10^{16}$ Hz and $\gamma = 3 \times 10^{14}$ Hz. The metal supports SPPs below the plasma frequency. An infinitely long antenna placed on the flat plasmonic metal serves as an SPP source when illuminated by light. The excited field distributions of SPPs are displayed in Fig. 1a. As the frequency increases, the propagation distance of the SPPs decreases, which means that SPPs at higher frequencies have shorter propagation lengths due to their stronger confinement to the interface. The corresponding Fourier

https://doi.org/10.1038/s41563-023-01787-8

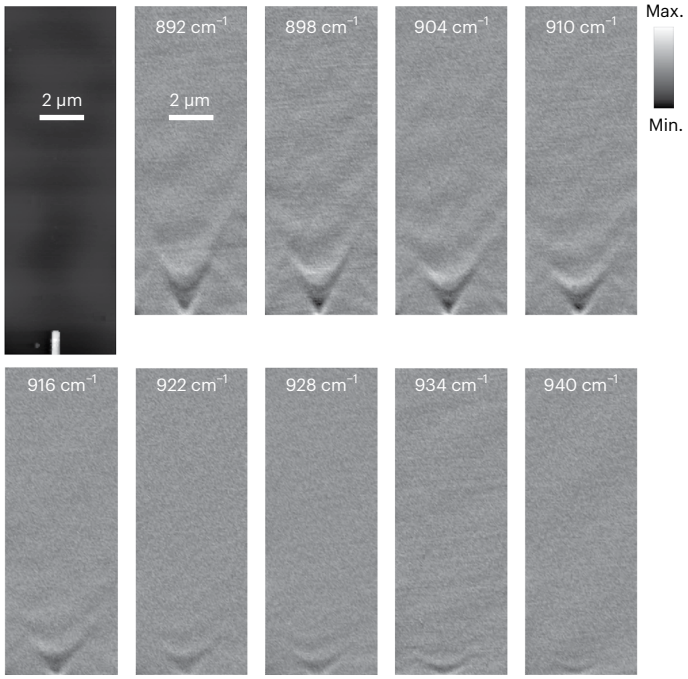

Fig. 2 | AFM (top left panel) and s-SNOM (other panels) imaging in the vicinity of an antenna on an MoO_3 film that supports hyperbolic PhPs. The excitation frequencies in the unit of wave numbers are labeled in each panel of the near-field distributions. Bright and dark colours correspond to maximum and minimum values.

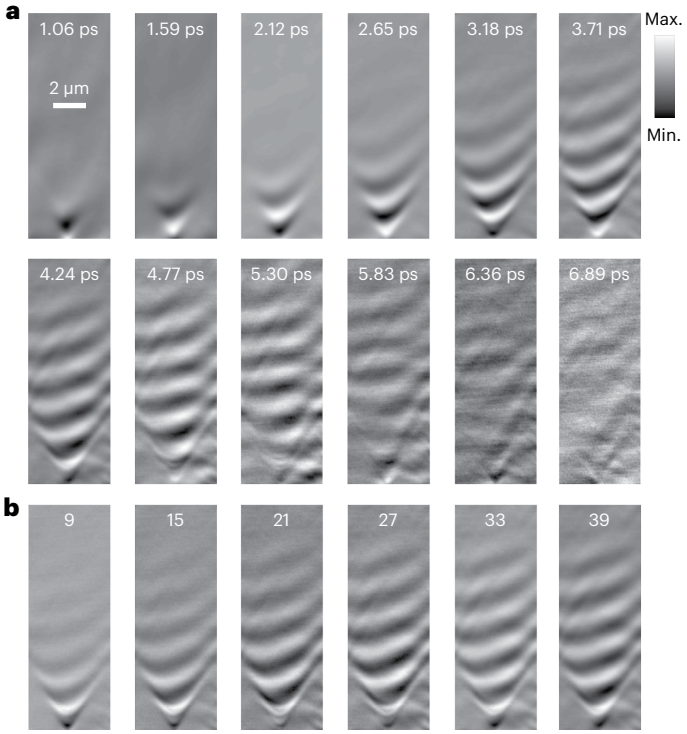

Fig. 3 | Synthetic s-SNOM imaging with a complex frequency of $\tilde{f} = (910 - 6.5\mathrm{i})$ cm^{-1} in different transient snapshots and at different synthesized real frequencies. a, The synthetic field in different transients with a total of 53 frequencies, ranging from 891 to 943 cm^{-1}. The temporal interval between the photographs is 0.53 ps, and the starting time is 1.06 ps. **b**, Imaging patterns with different numbers of synthetic frequencies, where the central frequency is fixed at 910 cm^{-1} and the frequency interval is fixed at 1 cm^{-1}. The patterns are labelled with their corresponding numbers of frequencies.

distributions of the SPPs are depicted in Fig. 1b. It is shown that the modes at high frequencies are blurred and eventually become invisible. The complex frequency can then be utilized to counterbalance the plasmonic loss and achieve complete loss compensation. The imaginary frequency f_i is calculated using equation (1) and plotted in Fig. 1c. It is shown that as the real frequency increases the imaginary frequency also increases monotonically to overcome the propagation loss. However, a complex frequency wave (temporally attenuated wave) is unphysical as the energy approaches infinity as time approaches negative infinity. Therefore, a truncation at the start of time is necessary to rationalize the complex frequency wave. The truncated complex frequency wave with temporal attenuation $e^{-i\tilde{\omega}t}\,\theta(t)$ can be transformed into the real frequency domain via Fourier transformation with θ(t) being the Heaviside step function: 0 for t <0 and 1 otherwise, and the corresponding spectrum distribution has a Lorentzian lineshape $1/(i\tilde{\omega} - i\omega')$ where ω′ is the real frequency. Thus, the complex frequency field distribution can be synthesized via linear combination of the real frequency field distributions as[32]

$$E(\tilde{\omega}, r, t) = \sum_i E\left(\omega_i', r\right) e^{-i\omega_i' t} \Delta\omega / \left(2\pi i\left(\tilde{\omega} - \omega_i'\right)\right) \qquad (2)$$

where the imaginary part of the complex frequency is obtained from equation (1). The dispersion under complex frequency excitation is shown in Fig. 1d, which fully recovers the dispersion at higher frequencies. The corresponding mathematical derivation and temporal evolution information are shown in Supplementary Section 2 and Supplementary Fig. 1. The dynamic evolution of the complex frequency excitation at $\tilde{f} = (700 - 6.73\mathrm{i})$ THz (its real part is indicated by the bottom dashed line in Fig. 1d) at different moments is depicted as Fig. 1e. An interesting observation is that as time increases the propagation distance extends linearly, but the amplitude remains uniform at different positions. This provides a direct visualization of lossless propagation of SPPs for a complex frequency excitation, which is in sharp contrast with that at the real frequency. The corresponding spatial field distribution at $t = 5.5 \times 10^{-2}$ ps is illustrated in the upper panel in Fig. 1f. We also plot the field distribution at a higher complex frequency $\tilde{f} = (850 - 17\mathrm{i})$ THz (indicated by the upper dashed line in Fig. 1d), with the result shown in the lower panel in Fig. 1f, which also shows much slower decay in comparison with the real frequency case.

The compensation of loss applies not only to metals described by the Drude model, but also to materials with more complicated dielectric functions, such as van der Waals materials that support PhPs. There is always a specific complex frequency solution for a PhP that satisfies Im(k) = 0. Here we consider a hexagonal boron nitride (hBN) film, which supports in-plane isotropic PhPs[43–47], and show that complex frequency can be utilized to compensate its intrinsic loss to observe lossless propagation of the PhP. The experimental set-up, based on the scattering-type scanning near-field optical microscopy (s-SNOM) technique, is illustrated in Fig. 1g. A long gold antenna placed on the hBN film is used to launch the one-dimensional PhPs (details in Supplementary Fig. 2). The electric field distributions are measured at frequencies ranging from 1,421 cm^{-1} to 1,503 cm^{-1}, with a step of 2 cm^{-1}, with all field plots provided in Supplementary Fig. 3. Two field distributions with real frequencies of 1,451 cm^{-1} and 1,477 cm^{-1} are chosen as the central frequencies to synthesize complex frequency responses at $\tilde{f}_1 = (1{,}451 - 4.5\mathrm{i})$ cm^{-1} and $\tilde{f}_2 = (1{,}477 - 6\mathrm{i})$ cm^{-1}. The corresponding imaginary part represents the optimized value at each frequency to achieve the longest propagation. The field distributions at the two real frequencies and at the corresponding complex frequencies are displayed in Fig. 1h,i, respectively. The experimental results demonstrate that, while the propagation at the real frequencies suffers strong attenuation, the polariton at the complex frequencies experiences almost no decay along the propagation.

https://doi.org/10.1038/s41563-023-01787-8

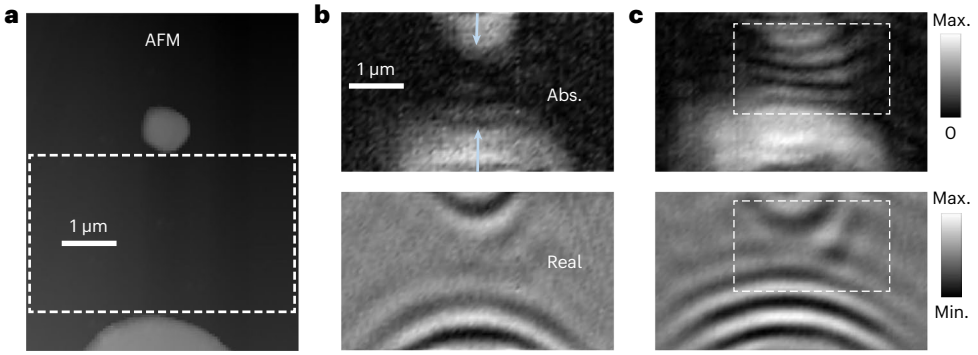

Fig. 4 | Investigation of interference of PhPs from two different circular antennas on MoO_3 flake. a, AFM image of the experimental sample. The bulges correspond to the positions of the antennas. **b**, The amplitude and real part of the near-field distribution at 990 cm^{-1} measured using s-SNOM. The scan region is in the dashed box of **a**. **c**, The amplitude and real part of the near field at the synthetic complex frequency $\tilde{f}$ = (990 − 2i) cm^{-1}, synthesized using a total of 26 frequencies; the corresponding temporal snapshot is 11.14 ps. The dashed boxes correspond to the strong-interference region.

We next apply the complex frequency approach to investigate the temporal evolution of more complicated field distributions supported by a thin film of van der Waals crystal α-MoO_3, which is highly anisotropic and supports natural in-plane hyperbolic polaritons[48–54]. A gold antenna is placed on the MoO_3 film to excite the PhPs, with the atomic force microscopy (AFM) image displayed in Fig. 2 (details in Supplementary Fig. 4). The near-field distributions on the MoO_3 interface measured by s-SNOM at different frequencies are shown in Fig. 2. The overall frequency range spans from 891 to 943 cm^{-1} with an interval of 1 cm^{-1}. Only nine field plots are presented in the figure while the others are displayed in Supplementary Figs. 5 and 6. The field distribution variation exhibits a characteristic hyperbolic propagation behaviour with a concave wavefront. With increasing frequency, the wavelength decreases with a stronger field confinement, and meanwhile the propagation becomes more attenuated. At all measured frequencies, the decay lengths of the polaritons are less than two wavelengths due to the significant intrinsic loss of the material.

We next insert all these electric field distributions, including both amplitude and phase information, into equation (2) to obtain the time-dependent field evolution with complex frequency. The synthesized electric field distributions at the complex frequency (910 − 6.5i) cm^{-1} and at different temporal moments are depicted in Fig. 3a, with a temporal step of 0.53 ps. Interestingly, for small t, the noise is largely smoothed by the summation of multifrequency signals. As time goes on, the wave travels farther and farther up, extending substantially beyond the decay length of two wavelengths at real frequencies. The two-dimensional field plot reaches its optimum at around 4.24 ps with the propagation length of 8.7 μm (along the vertical direction), while the corresponding propagation length of the central real frequency is only 1.6 μm. Thus, the propagation length under this complex frequency approach is increased more than fourfold compared with that of the central real frequency. Other complex frequency results are displayed in Supplementary Fig. 7, and all show much longer propagation distance than the corresponding real frequencies. On further increasing t, the noise starts to become dominant, as the signal continues to attenuate in the time domain. As time exceeds 4.77 ps, the field distribution begins to exhibit chaotic behaviour. A dynamic representation of spatiotemporal evolution is shown in Supplementary Video 1. It should be noted that the longer the propagation time the greater the propagation distance, but the magnitude of the signal field becomes weaker. When the magnitude of the signal field drops to the same level as that of the noise, the signal carried by the polariton will be distorted by the noise. Thus, there exists a trade-off between the longer propagation and the signal–noise ratio when deciding the optimal time for constructing waves in the complex frequency domain.

The effect of the number of frequency points is also investigated, as shown in Fig. 3b, with the frequency step fixed at 1 cm^{-1} and the temporal snapshot fixed at 4.24 ps. It is evident that the field plot with nine frequency points is already substantially improved compared with that of real frequency. As the number of frequencies increases to 21, the decay length continues to increase. However, further increasing the number to 39 does not provide obvious improvement.

We further apply the complex frequency approach to investigate the interference behaviour of PhPs. Two circular antennas with different diameters (~0.8 μm and ~3 μm) are fabricated on the MoO_3 film (details in Supplementary Fig. 8) to excite the PhPs, as shown in Fig. 4a. The field distribution inside the white dashed box is scanned using an s-SNOM probe, with the amplitude and real part of the electric field distribution at a frequency of f = 990 cm^{-1} shown in the top and bottom panels of Fig. 4b, respectively. The PhPs emanating from the two antennas propagate towards each other, but they do not form discernible interference fringes due to the strong attenuation. By synthesizing the field plots at the complex frequency $\tilde{f}$ = (990 − 2i)cm^{-1}, the intrinsic loss in the MoO_3 film is compensated for, thereby enabling longer propagation of PhPs. This facilitates the formation of clear interference patterns between the antennas, as shown by Fig. 4c. The dynamic behaviour is displayed in Supplementary Video 2, which exhibits the interesting features of a negative phase velocity and a slow group velocity, because of the negative slope of dispersion of the PhPs across this frequency range. All the measured field distributions at different real frequencies for constructing the synthesized complex frequency field plot are provided in Supplementary Figs. 9 and 10.

In conclusion, we have implemented the complex frequency approach to dramatically enhance the decay length of highly confined PhPs, achieving nearly complete loss compensation that is only limited by the noise level. This concept is general and can be easily extended to other frequency regimes and to other types of wave, including acoustic and elastic waves. The ability to achieve loss compensation for propagation of PhPs via virtual gain has significant implications for a wide range of applications, including the development of photonic integrated circuits, where the ability to transmit information over longer distances is critical for ensuring the performance and reliability of the circuit.

Online content

Any methods, additional references, Nature Portfolio reporting summaries, source data, extended data, supplementary information, acknowledgements, peer review information; details of author contributions and competing interests; and statements of data and code availability are available at https://doi.org/10.1038/s41563-023-01787-8.

References

1. Barnes, W. L., Dereux, A. & Ebbesen, T. W. Surface plasmon subwavelength optics. *Nature* **424**, 824–830 (2003).
2. Oulton, R. F. et al. Plasmon lasers at deep subwavelength scale. *Nature* **461**, 629–632 (2009).
3. Gramotnev, D. K. & Bozhevolnyi, S. I. Plasmonics beyond the diffraction limit. *Nat. Photon.* **4**, 83–91 (2010).
4. Basov, D. N., Fogler, M. M. & García De Abajo, F. J. Polaritons in van der Waals materials. *Science* **354**, aag1992 (2016).
5. Low, T. et al. Polaritons in layered two-dimensional materials. *Nat. Mater.* **16**, 182–194 (2017).
6. Wei, H., Wang, Z., Tian, X., Käll, M. & Xu, H. Cascaded logic gates in nanophotonic plasmon networks. *Nat. Commun.* **2**, 387 (2011).
7. Fu, Y. et al. All-optical logic gates based on nanoscale plasmonic slot waveguides. *Nano Lett.* **12**, 5784–5790 (2012).
8. Zhang, Q. et al. Interface nano-optics with van der Waals polaritons. *Nature* **597**, 187–195 (2021).
9. Stockman, M. I. Nanofocusing of optical energy in tapered plasmonic waveguides. *Phys. Rev. Lett.* **93**, 137404 (2004).
10. Prodan, E., Radloff, C., Halas, N. J. & Nordlander, P. A hybridization model for the plasmon response of complex nanostructures. *Science* **302**, 419–422 (2003).
11. Woessner, A. et al. Highly confined low-loss plasmons in graphene–boron nitride heterostructures. *Nat. Mater.* **14**, 421–425 (2015).
12. Arakawa, E. T., Williams, M. W., Hamm, R. N. & Ritchie, R. H. Effect of damping on surface plasmon dispersion. *Phys. Rev. Lett.* **31**, 1127–1129 (1973).
13. Bozhevolnyi, S. I., Volkov, V. S., Devaux, E., Laluet, J.-Y. & Ebbesen, T. W. Channel plasmon subwavelength waveguide components including interferometers and ring resonators. *Nature* **440**, 508–511 (2006).
14. Anker, J. N. et al. Biosensing with plasmonic nanosensors. *Nat. Mater.* **7**, 442–453 (2008).
15. Rodrigo, D. et al. Mid-infrared plasmonic biosensing with graphene. *Science* **349**, 165–168 (2015).
16. Yang, X. et al. Nanomaterial-based plasmon-enhanced infrared spectroscopy. *Adv. Mater.* **30**, 1704896 (2018).
17. Bylinkin, A. et al. Real-space observation of vibrational strong coupling between propagating phonon polaritons and organic molecules. *Nat. Photon.* **15**, 197–202 (2021).
18. Fang, N., Lee, H., Sun, C. & Zhang, X. Sub-diffraction-limited optical imaging with a silver superlens. *Science* **308**, 534–538 (2005).
19. Liu, Z., Lee, H., Xiong, Y., Sun, C. & Zhang, X. Far-field optical hyperlens magnifying sub-diffraction-limited objects. *Science* **315**, 1686 (2007).
20. Li, P. et al. Hyperbolic phonon-polaritons in boron nitride for near-field optical imaging and focusing. *Nat. Commun.* **6**, 7507 (2015).
21. Dai, S. et al. Subdiffractional focusing and guiding of polaritonic rays in a natural hyperbolic material. *Nat. Commun.* **6**, 6963 (2015).
22. Wei, F. & Liu, Z. Plasmonic structured illumination microscopy. *Nano Lett.* **10**, 2531–2536 (2010).
23. Yan, H. et al. Damping pathways of mid-infrared plasmons in graphene nanostructures. *Nat. Photon.* **7**, 394–399 (2013).
24. Ni, G. X. et al. Fundamental limits to graphene plasmonics. *Nature* **557**, 530–533 (2018).
25. Anantha Ramakrishna, S. & Pendry, J. B. Removal of absorption and increase in resolution in a near-field lens via optical gain. *Phys. Rev. B* **67**, 201101 (2003).
26. Xiao, S. et al. Loss-free and active optical negative-index metamaterials. *Nature* **466**, 735–738 (2010).
27. Hess, O. et al. Active nanoplasmonic metamaterials. *Nat. Mater.* **11**, 573–584 (2012).
28. Stockman, M. I. Spaser action, loss compensation, and stability in plasmonic systems with gain. *Phys. Rev. Lett.* **106**, 156802 (2011).
29. Pendry, J. B. & Maier, S. A. Comment on 'Spaser action, loss compensation, and stability in plasmonic systems with gain'. *Phys. Rev. Lett.* **107**, 259703 (2011).
30. Wuestner, S., Pusch, A., Tsakmakidis, K. L., Hamm, J. M. & Hess, O. Comment on 'Spaser action, loss compensation, and stability in plasmonic systems with gain'. *Phys. Rev. Lett.* **107**, 259701 (2011).
31. Archambault, A., Besbes, M. & Greffet, J. J. Superlens in the time domain. *Phys. Rev. Lett.* **109**, 097405 (2012).
32. Guan, F. et al. Overcoming losses in superlenses with synthetic waves of complex frequency. *Science* **771**, 766–771 (2023).
33. Kim, S., Peng, Y., Yves, S. & Alù, A. Loss compensation and super-resolution with excitations at complex frequencies. *Phys. Rev. X* **13**, 041024 (2023).
34. Tetikol, H. S. & Aksun, M. I. Enhancement of resolution and propagation length by sources with temporal decay in plasmonic devices. *Plasmonics* **15**, 2137–2146 (2020).
35. Kirby, E. I., Hamm, J. M., Pickering, T. W., Tsakmakidis, K. L. & Hess, O. Evanescent gain for slow and stopped light in negative refractive index heterostructures. *Phys. Rev. B* **84**, 041103 (2011).
36. Ciattoni, A., Marini, A., Rizza, C., Scalora, M. & Biancalana, F. Polariton excitation in epsilon-near-zero slabs: transient trapping of slow light. *Phys. Rev. A* **87**, 053853 (2013).
37. Tsakmakidis, K. L., Pickering, T. W., Hamm, J. M., Page, A. F. & Hess, O. Completely stopped and dispersionless light in plasmonic waveguides. *Phys. Rev. Lett.* **112**, 167401 (2014).
38. Tsakmakidis, K. L., Baskourelos, K. G. & Wartak, M. S. *Metamaterials and Nanophotonics* (World Scientific, 2022).
39. Baranov, D. G., Krasnok, A. & Alù, A. Coherent virtual absorption based on complex zero excitation for ideal light capturing. *Optica* **4**, 1457–1461 (2017).
40. Kim, S., Lepeshov, S., Krasnok, A. & Alù, A. Beyond bounds on light scattering with complex frequency excitations. *Phys. Rev. Lett.* **129**, 203601 (2022).
41. Li, H., Mekawy, A., Krasnok, A. & Alù, A. Virtual parity-time symmetry. *Phys. Rev. Lett.* **124**, 193901 (2020).
42. Gu, Z. et al. Transient non-Hermitian skin effect. *Nat. Commun.* **13**, 7668 (2022).
43. Li, N. et al. Direct observation of highly confined phonon polaritons in suspended monolayer hexagonal boron nitride. *Nat. Mater.* **20**, 43–48 (2021).
44. Dai, S. et al. Tunable phonon polaritons in atomically thin van der Waals crystals of boron nitride. *Science* **343**, 1125–1130 (2014).
45. Yoxall, E. et al. Direct observation of ultraslow hyperbolic polariton propagation with negative phase velocity. *Nat. Photon.* **9**, 674–678 (2015).
46. Kurman, Y. et al. Spatiotemporal imaging of 2D polariton wave packet dynamics using free electrons. *Science* **372**, 1181–1186 (2021).
47. Guo, X. et al. Hyperbolic whispering-gallery phonon polaritons in boron nitride nanotubes. *Nat. Nanotechnol.* **18**, 529–534 (2023).
48. Zheng, Z. et al. Highly confined and tunable hyperbolic phonon polaritons in van der Waals semiconducting transition metal oxides. *Adv. Mater.* **30**, 1705318 (2018).
49. Hu, G. et al. Topological polaritons and photonic magic angles in twisted α-MoO_3 bilayers. *Nature* **582**, 209–213 (2020).
50. Ma, W. et al. In-plane anisotropic and ultra-low-loss polaritons in a natural van der Waals crystal. *Nature* **562**, 557–562 (2018).
51. Guo, X. et al. Mid-infrared analogue polaritonic reversed Cherenkov radiation in natural anisotropic crystals. *Nat. Commun.* **14**, 2532 (2023).

52. Wang, M. et al. Spin–orbit-locked hyperbolic polariton vortices carrying reconfigurable topological charges. *eLight* **2**, 12 (2022).
53. Hu, C. et al. Source-configured symmetry-broken hyperbolic polaritons. *eLight* **3**, 14 (2023).
54. Huang, W. et al. In-plane hyperbolic polariton tuners in terahertz and long-wave infrared regimes. *Nat. Commun.* **14**, 2716 (2023).

Methods

High-quality hBN and MoO_3 flakes were obtained by mechanically exfoliating the corresponding bulk crystals. These flakes were subsequently transferred using a polydimethylsiloxane stamp onto Si wafers coated with a thin film of SiO_2 of 280 nm thickness, or gold substrates. Then gold antennas were patterned on the MoO_3 and hBN flakes using electron-beam lithography followed by a lift-off process. The lift-off process consists of deposition of 10 nm Cr and 100 nm Au using an electron beam in a vacuum chamber, and removal of the polymethylmethacrylate in a hot acetone bath (60 °C, 40 min) followed by a gentle washing with isopropyl alcohol. The morphologies of the samples are illustrated in Supplementary Figs. 2, 4 and 8.

The near-field measurement was performed using a scattering scanning near-field optical microscope (neaspec) combined with a widely tunable mid-infrared optical parametric oscillator laser (550–2,200 cm^{-1}). A parabolic mirror was employed to focus the p-polarized incident beam onto both the AFM tip and sample at an incident angle of 52°. The AFM tip has an apex radius in the range 10–20 nm. The tapping frequency of the tip was around 270 kHz, with amplitudes ranging from 50 to 100 nm. To remove the influence of the background on the near-field scattering, we combined interferometric measurement of the light backscattered by the tip with demodulation of the detected signal at multiples of the tapping frequency (typically second or third harmonics). The amplitude and phase of the signal can be independently obtained via phase modulation of the reference beam. For more detailed information, please refer to Supplementary Section 3 and Supplementary Fig. 11.

The electromagnetic simulations were performed using the commercial full-wave finite-element method software COMSOL Multiphysics. A flat interface of air/dispersive Drude model with $\varepsilon_m = 5 - (1.44 \times 10^4\ \mathrm{THz})^2/[\omega^2 + (3 \times 10^2\ \mathrm{THz})i\omega]$ supports SPPs composed of both x- and y-polarized electric field. A metal antenna, 80 nm in width, was placed on the two-dimensional interface, and normally illuminated with an x-polarized plane wave to excite the SPPs on the interface. Perfectly matched layer boundaries were employed in both x and y directions in the two-dimensional simulation to absorb the clutter waves. The simulation frequency range was swept from 500 to 1,030 THz with a frequency gap of 0.5 THz. We recorded the y-polarized electric field of each frequency just above the interface to synthesize the complex frequency wave.

Data availability

The data that support the findings of this study are available within this Article and the Supplementary Information.

Code availability

The code that supports the findings of this study is available from the corresponding author upon reasonable request.

Acknowledgements

This work was supported by New Cornerstone Science Foundation and the Research Grants Council of Hong Kong, AoE/P-701/20, 17315522, A-HKU705/21 (to Shuang Zhang), the National Natural Science Foundation of China (51925203 to Q.D.; 52022025 to X.Y. and 52102160 to X.G.) and the Young Elite Scientists Sponsorship Program by CAST, 2022QNRC001 (to X.G.).

Author contributions

Shuang Zhang, F.G., Q.D. and X.G. conceived the project. F.G. and X.G. designed the experiments. X.G. and Shu Zhang prepared the experimental samples and performed the s-SNOM experiments with the help of C.W.; F.G. and X.G. analysed the experimental data and performed the simulation. F.G., X.G., Shu Zhang, K.Z., Y.H., Y.X., S. Zhou, X.Y., Q.D. and Shuang Zhang participated in the analysis of the results. F.G., X.G. and Shuang Zhang wrote the manuscript with input from all authors. Shuang Zhang and Q.D. supervised the overall projects. All authors contributed to the discussion.

Competing interests

The authors declare no competing interests.

Additional information

Supplementary information The online version contains supplementary material available at https://doi.org/10.1038/s41563-023-01787-8.

Correspondence and requests for materials should be addressed to Qing Dai or Shuang Zhang.

Peer review information *Nature Materials* thanks the anonymous reviewers for their contribution to the peer review of this work.